Single-crystalline transition metal phosphide superconductor WP studied by Raman spectroscopy and first-principles calculations

Yanmin Zhang [1,*] Luo Yan,[2] Wei Wu,[1,3,†] Ge He [4] Jingsong Zhang,[1,3] Zhuang Ni,[1,3] Xingyu Jiang,[1,3] Mingyang Qin,[1,3] Feng Jin,[1] Jie Yuan [1,3,5] Beiyi Zhu,[1] Qihong Chen,[1] Liujiang Zhou,[2] Yangmu Li,[1,3] Jianlin Luo,[1,3,5] and Kui Jin [1,3,5]

[1]*Beijing National Laboratory for Condensed Matter Physics, Institute of Physics, Chinese Academy of Sciences, Beijing 100190, China*
[2]*School of Physics, University of Electronic Science and Technology of China, Chengdu 610054, China*
[3]*School of Physical Sciences, University of Chinese Academy of Sciences, Beijing 100049, China*
[4]*Walther Meissner Institute, Bayerische Akademie der Wissenschaften, 85748 Garching, Germany*
[5]*Songshan Lake Materials Laboratory, Dongguan, Guangdong 523808, China*

We present a study of phonon modes and electron-phonon coupling in superconductor WP using angle-resolved polarized Raman spectroscopy. Seven out of twelve Raman-active modes are detected, with frequencies in good accordance by the first-principles calculations. We analyze parallel- and cross-polarized configurations of A_g and B_{3g} phonon modes with polarization- and angle-resolved Raman measurements. For the observed seven modes, the total electron-phonon coupling parameter λ is only about 0.07, which is too small to achieve superconductivity. Our results elucidate that the low-frequency phonon modes play a key role in the superconductivity within the Bardeen-Cooper-Schrieffer theory framework.

I. INTRODUCTION

Transition-metal pnictides have attracted much attention for quite a few years due to their unique physical properties, such as superconductivity [1,2], topological structure [3,4], and potential application of chirality memory [5,6]. Most of the transition-metal pnictides MX (M = transition metal, X = P, As, Sb) belong to the hexagonal NiAs-type or orthorhombic MnP-type structure [7]. Tremel *et al*. [8] reported that orthorhombic MnP-type phases can only exist in the transition-metal phosphide compounds MP with a large number of valence electrons, such as CrP, WP, MnP, FeP, RuP, CoP, and IrP. Among these phosphides, Rh-doped RuP has a superconducting transition temperature $T_c = 3.7$ K [9] and MnP exhibits superconductivity at $\sim$ 1 K under 8 GPa [10]. Recently, superconductivity was reported in WP, which is the first superconductor among 5d-transition metal pnictides at ambient pressure [11], exhibiting a relatively large orbital overlap and complex band structure. In addition, WP was predicted to be a topological nonsymmorphic crystalline superconductor by theoretical studies [12].

Previous studies [11,13] show that WP is a weak coupled Bardeen-Cooper-Schrieffer (BCS) superconductor with a small electron-phonon coupling (EPC) strength ($\lambda_{ep} \sim$ 0.453, from the normal-state resistivity; $\lambda_{ep} \sim$ 0.365, from specific-heat) [11], but the contribution of different phonon modes to superconductivity has not been studied due to the lack of single crystals with large size. Here we present a systematic study on superconducting WP by angle-resolved

polarized Raman spectroscopy (ARPRS) and first-principles calculations. Seven Raman-active phonon modes have been observed with frequencies matching well with our calculated values. After further calculations, it is discovered that the low-frequency phonon modes contribute a large part (76%) to EPC. We measured the Raman-active modes, a part of optical modes, and this part does not contribute much to the EPC. We found that although the A_g-4 mode has an asymmetric line shape, it has little contribution to the superconductivity. The experimental Raman data are consistent with the calculations.

II. EXPERIMENT

High-quality WP single crystals with T_c of $\sim$ 0.84 K used in our Raman study were grown by the chemical vapor transport method [11]. The single crystallinity of WP sample with a size of $0.25 \times 0.11 \times 3.95$ mm³ has been characterized by x-ray diffraction measurement. Raman data were recorded by the microscope Raman spectrometer system (300 K, LabRAM HR Evolution, Horiba Jobin Yvon) with the excitation wavelength of 532 nm (polarization extinction ratio >1000:1, Oxxius, France). A 0.9 NA 100× objective lens was used to focus the laser beam and collect the back-scattered Raman signal. Temperature-dependent Raman spectra were acquired by cooling the sample in a liquid helium-free cryostat (5.6–300 K, Montana Instruments microReveal Raman, Quantum Design). As shown in Fig. 1(a), we define x, y, and z as the directions along the unit cell axes. Raman spectra have been recorded under polarization configurations of both (yy) and (yz). Figure 1(b) shows the schematics of the ARPRS measurements. A half-wave ($\lambda/2$) plate [14] was placed in the common optical path of an incident laser and scattered Raman

*Corresponding author: yanminzhang@iphy.ac.cn
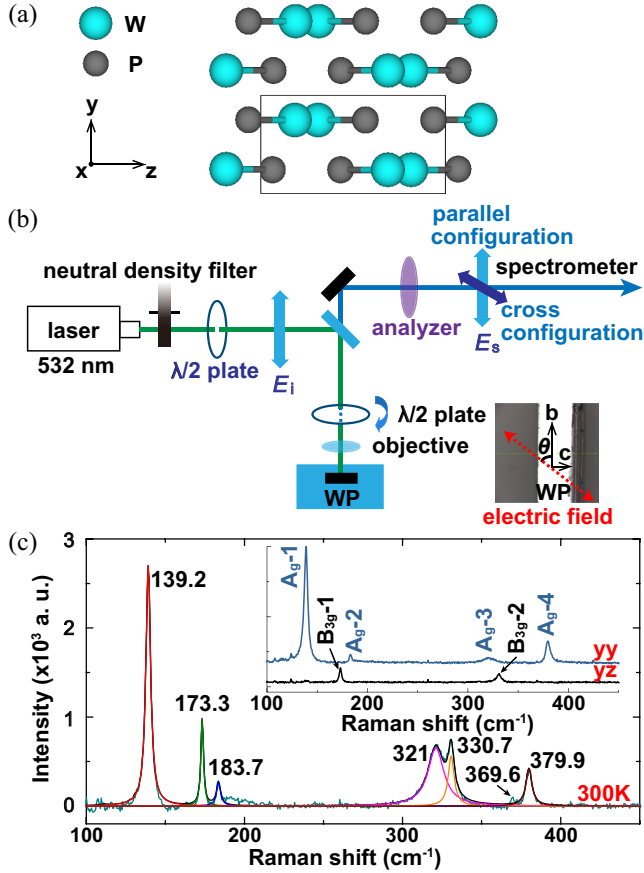†Corresponding author: welyman@iphy.ac.cn

FIG. 1. (a) Crystal structure of WP in yz plane. We defined x, y, and z as the directions along the unit cell a, b, and c axes, respectively. (b) Schematic of the ARPRS. The electric field of the linearly polarized incident and the scattered light are E_i and E_s, respectively. The bottom-right inset depicts the optical image of the WP single crystal measured by ARPRS. The angle θ was defined as the angle between the light polarization direction and the b axis. (c) Raman spectra of the WP. The colored curves are the resulting fitted spectra with Lorentz functions. The upper-right inset shows Raman spectra of the WP which were measured in the (yy) parallel-polarized (i.e., $E_i \parallel E_s \parallel b$-axis) and ($yz$) cross-polarized (i.e., $E_i \perp E_s$, $E_i \parallel b$-axis, and $E_s \parallel c$-axis) configurations, respectively.

signal to simultaneously vary their polarization directions instead of rotating the sample in the yz plane.

WP belongs to space group *Pnma* (point group D_{2h}) [11], as shown in Fig. 1(a). A unit cell contains one primitive cell, with eight atoms in total. A factor group symmetry analysis [15,16] indicates that the phonon modes at Brillouin zone (BZ) center Γ should be decomposed into 24 irreducible representations: $[B_{1u} + B_{2u} + B_{3u}] + [4A_g + 2B_{1g} + 4B_{2g} + 2B_{3g}] + [3B_{1u} + B_{2u} + 3B_{3u}] + 2A_u$, where the first, second, and third terms represent the acoustic modes, Raman-active modes, and infrared-active modes, respectively. The $2A_u$ modes are inactive in both Raman and infrared spectra. To estimate phonon frequencies, we performed first-principles calculations of the phonon modes at Γ in the framework of density functional theory (DFT) [17,18] with spin-orbit coupling. We adopted the fully relaxed lattice parameters $a = 5.76$ Å, $b = 3.27$ Å and $c = 6.26$ Å

TABLE I. The calculated 21 optical phonon modes including Raman-active (Raman), infrared-active (IR), and inactive phonon modes, and experimental Raman-active phonon modes of WP.

Symmetry	Activity	Calculated energy /cm^{-1}	Experimental energy /cm^{-1}
B_{3u}	IR	125.1	
B_{1g}	Raman	128.4	
A_g	Raman	136.7	139.2
A_u	inactive	146.4	
B_{1u}	IR	154.2	
B_{2g}	Raman	162.7	
B_{3g}	Raman	172.5	173.3
A_g	Raman	182.8	183.7
B_{2g}	Raman	191.7	
B_{1u}	IR	299.3	
A_g	Raman	317.1	321.0
B_{2u}	IR	323.9	
B_{3g}	Raman	324.4	330.7
A_u	inactive	331.6	
B_{3u}	IR	334.0	
B_{1g}	Raman	352.3	
B_{2g}	Raman	371.5	369.6
A_g	Raman	373.9	379.9
B_{1u}	IR	403.9	
B_{2g}	Raman	409.1	
B_{3u}	IR	420.4	

determined by a single-crystal x-ray diffractometer (Bruker D8 VENTURE), and the Wyckoff positions (W 4c and P 4c) from experimental data [11]. For all calculations, we used the VIENNA AB INITIO SIMULATION PACKAGE [19] and the QUANTUM ESPRESSO (QE) code. The DFT calculations employ the Perdew-Burke-Ernzerhof exchange-correlation functional [20] in the projector augmented-wave implementation [21]. A plane-wave cutoff energy of 450 eV was used with a uniform $6 \times 6 \times 6$ Monkhorst-Pack [22] k-point mesh for eight supercells. The phonon frequencies were calculated from the force constants using the PHONOPY code [23]. The calculated optical mode energy, their symmetries, and optical activities are given in Table I. Our calculation results are consistent with the experimental values. The EPC and superconductivity were calculated by the QE within the density functional perturbation theory [24] and BCS theory [25]. The optimized norm-conserving Vanderbilt pseudopotentials [26] were used to model the electron-ion interactions. The kinetic energy cutoff and the charge density cutoff of the plane-wave basis were chosen to be 70 and 280 Ry, respectively. Self-consistent electron density was evaluated by employing $24 \times 24 \times 1$ **k** mesh with a Methfessel-Paxton smearing width of 0.02 Ry. The phonon calculations were carried out on the $6 \times 3 \times 3$ **q** mesh.

III. RESULTS

As we can see from Fig. 1(c), the Raman spectra of WP with seven peaks can be observed in the range of 100–400 cm^{-1}. The inset in Fig. 1(c) depicts the polarized Raman spectra of WP. Four peaks can be observed in the (yy)

configuration, while two peaks are presented in the (yz) configuration. The Raman tensors R corresponding to the symmetry group are expressed in the xyz coordinates as

$$A_g = \begin{pmatrix} a & 0 & 0 \\ 0 & b & 0 \\ 0 & 0 & c \end{pmatrix}, \quad B_{1g} = \begin{pmatrix} 0 & d & 0 \\ d & 0 & 0 \\ 0 & 0 & 0 \end{pmatrix},$$

$$B_{2g} = \begin{pmatrix} 0 & 0 & e \\ 0 & 0 & 0 \\ e & 0 & 0 \end{pmatrix}, \quad B_{3g} = \begin{pmatrix} 0 & 0 & 0 \\ 0 & 0 & f \\ 0 & f & 0 \end{pmatrix}. \quad (1)$$

According to the polarization selection rules, the peaks appearing both under (yy) or (zz) polarization configurations are A_g modes, while the peaks appearing only under (yz) polarization configuration should be B_{3g} modes. It is straightforward to assign the four peaks at 139.2 cm^{-1}, 183.7 cm^{-1}, 321 cm^{-1}, 379.9 cm^{-1} to A_g modes, which are detected under (yy) polarization configuration. Two peaks at 173.3 cm^{-1} and 330.7 cm^{-1} are B_{3g} modes. Therefore, four A_g and two B_{3g} phonon modes can be obtained under (yy) and (yz) configurations. In principle, B_{1g} and B_{2g} modes cannot be detected in our experiments. The small peak with weak intensity observed at 369.6 cm^{-1} is the B_{2g} mode at 371.5 cm^{-1}, predicted by calculation, where the leakage of the forbidden B_{2g} mode is due to the slight deviation between polarization direction and crystal axis.

To further explore the anisotropic phonon vibration modes in WP, we summarize the intensities of these six peaks with different rotation angles under parallel- and cross-polarized configurations in Fig. 2. It is obvious that intensities of the five peaks exhibit strong angle-dependent behavior as demonstrated by the contour color map under parallel- and cross-polarized configurations [Figs. 2(a) and 2(b)]. The angle dependence of the six observed Raman modes are displayed in Figs. 2(c)–2(n). We notice the following features: (i) The peak intensities of A_g-1, A_g-3, and A_g-4 modes show twofold symmetry under the parallel-polarized configuration with a changing rotation angle of the half-wave plate, while two B_{3g} modes show a different variation rule. (ii) The intensities of both A_g and B_{3g} modes show fourfold symmetry under the cross-polarized configuration. (iii) In addition, the peak intensity of A_g-2 is almost angle independent under the parallel-polarized configuration.

The anisotropic Raman spectra of WP can be well understood within the classical Placzek model, where the Raman scattering intensity can be described by $I \propto |e_i \cdot R \cdot e_s|^2$ [27], where e_i and e_s are the unit polarization vectors of the incident and scattered lights, respectively, and R is the Raman tensor for the Raman-active modes of WP. The incident light polarization $e_i = (0, \cos\theta, \sin\theta)$ becomes $e_{s,\parallel} = (0, \cos\theta, \sin\theta)^T$ (under parallel-polarized configuration) and $e_{s,\perp} = (0, -\sin\theta, \cos\theta)^T$ (under cross-polarized configuration) after scattered [28]. The Raman tensor of WP can be described as $R_{WP}(A_g,$

$$B_{1g}, B_{2g}, B_{3g}) = \begin{pmatrix} a & d & e \\ d & b & f \\ e & f & c \end{pmatrix}.$$

Herein, only A_g and B_{3g} modes can be detected due to the nonzero values in the Raman tensors. Thus the Raman
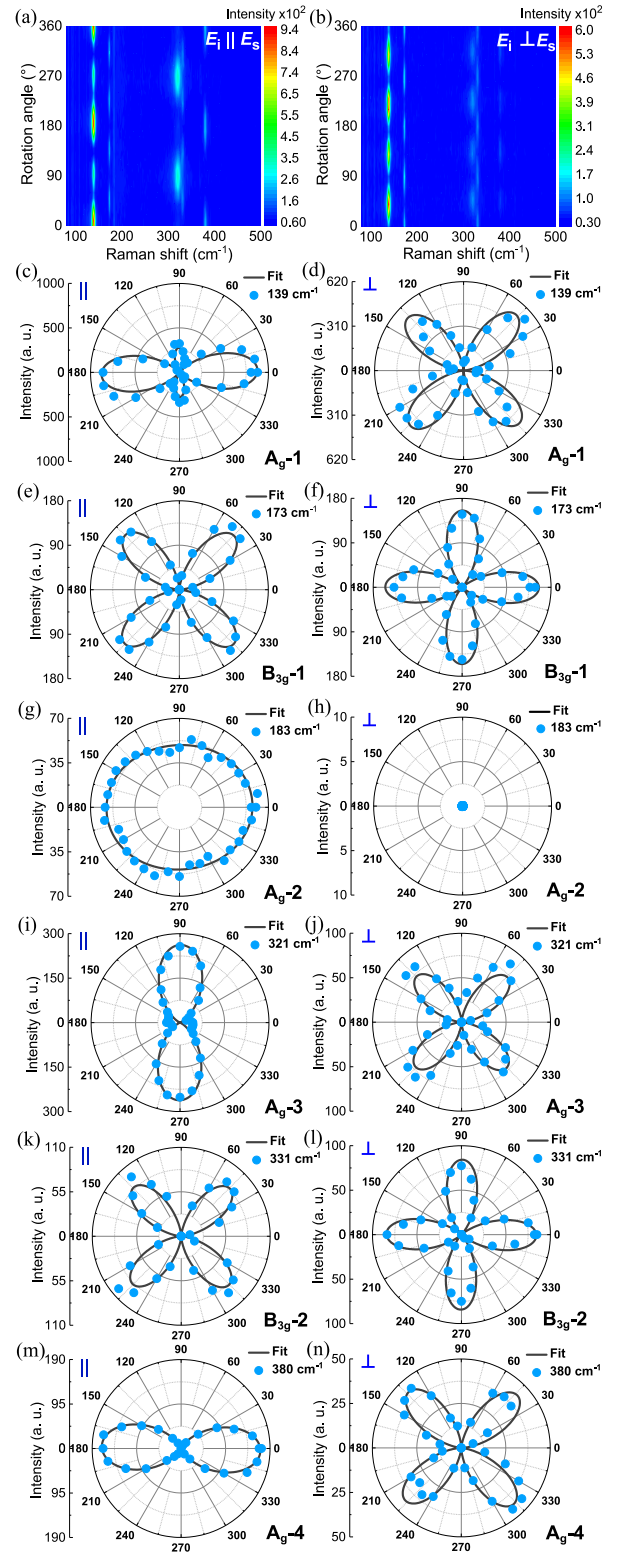

FIG. 2. Angle-dependent Raman spectra of the measured WP single crystal. Contour map of the measured Raman phonon intensities as a function of angle and energy under parallel- and cross-polarized configurations [(a), (b)]. Angle dependence of the Raman-active phonon peak intensities measured in parallel-polarized [(c), (e), (g), (i), (k), (m)] and cross-polarized [(d), (f), (h), (j), (l), (n)] configurations. The blue dots show the measured data. The black solid curves display the fit results based on Eqs. (2)–(5).

scattering intensities of A_g and B_{3g} modes can be further expressed by [29]

$$I(A_g, \parallel) = (b\cos^2\theta + c\sin^2\theta)^2, \tag{2}$$

$$I(A_g, \perp) = \frac{(c-b)^2}{4}\sin^2 2\theta, \tag{3}$$

$$I(B_{3g}, \parallel) = f^2\sin^2 2\theta, \tag{4}$$

$$I(B_{3g}, \perp) = f^2\cos^2 2\theta. \tag{5}$$

The angle-dependent Raman scattering intensities can be well fitted with Eqs. (2)–(5). It is apparently observed that A_g modes show either marked twofold symmetry or angle independence under the parallel-polarized configuration, while B_{3g} modes exhibit fourfold symmetry. Except for the A_g-2 mode, with fit parameters $b = 7$, $c = 7.6$, $I < 0.1$, all these modes show fourfold symmetry under cross-polarized configuration. The intensities calculated from the above equations always reach the maximum at $\theta = 0°$ and $90°$ under the parallel-polarized configuration. Thus, the crystalline orientation of the WP can be determined by the A_g mode.

We notice that the A_g-1 and A_g-4 modes of WP seem to have asymmetric line shapes, which implies a Fano resonance. The Fano resonance is a quantum interference between a discrete state and a continuum one [30]. For Raman scattering, the spectrum of the phonon mode presents an asymmetric Fano line shape if there is an EPC [31,32]. In the pressure-induced superconductor CrAs [7], which also features a MnP structure, Fano asymmetry line shapes cannot be detected for four A_g modes, indicating weak coupling between these phonons and any electronic continuum in CrAs [33]. We analyzed the Raman spectra of A_g-1 and A_g-4 modes of WP in Fig. 3(a) with the Fano function. The Raman spectra can be well fitted by the equation

$$I(\omega) = A\frac{(q\gamma/2 + \omega - \omega_0)^2}{(\gamma/2)^2 + (\omega - \omega_0)^2}, \tag{6}$$

where A is amplitude, ω_0 is resonance energy (renormalized in the presence of the coupling), γ is linewidth (full width at half maximum), and q is the asymmetric parameter. The factor $|1/q|$ is often used to estimate the EPC strength [34–37]. The larger the $|1/q|$, the stronger the coupling. We get $q = -24.2$ for the A_g-1 mode and $q = -0.08$ for the A_g-4 mode. It is indicated that the A_g-1 mode has almost no EPC. Furthermore, the temperature dependence of the Raman spectrum of the A_g-4 mode is shown in Fig. 3(b). The A_g-4 mode has higher energies upon cooling. The fit results including the renormalized phonon energies ω_0, the linewidths γ, and the Fano asymmetry parameters q are displayed in Figs. 3(c)–3(e). We can see that the linewidth of the A_g-4 mode is very narrow ($\sim 6\ \text{cm}^{-1}$) and changes slightly with temperature. The renormalized phonon energies ω_0 change $\sim 2\ \text{cm}^{-1}$ from 5.6 to 300 K by careful measurement. We note that the A_g-4 mode exhibits similar behavior from 10 to 265 K in CrAs [33].

To further study the role of the EPC in WP, we estimate EPC strength of the A_g-4 mode by Allen's formula [38–40],

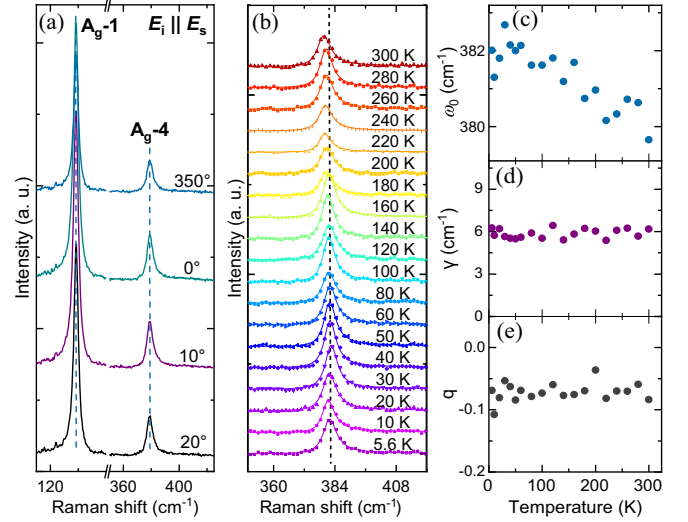$$\lambda_i = \frac{2g_i\gamma_i}{\pi N_{\epsilon f}\omega_i^2}, \tag{7}$$

FIG. 3. (a) Raman spectra for A_g-1 and A_g-4 modes of WP at $\theta = 20°$, $10°$, $0°$, and $350°$ under parallel-polarized configuration. (b) Waterfall plot of temperature-dependent Raman spectra for A_g-4 mode of WP. The vertical dashed lines indicate the A_g-4 mode. The colored dots with different shaped curves are the experimental data at the corresponding temperature. The colored curves are the resulting fitted spectra with Fano functions. (c) Temperature evolution of the phonon energies ω_0. (d) Temperature evolution of the linewidth γ. (e) Fano symmetry parameter q of the A_g-4 mode from the fit in (b).

where λ_i is dimensionless EPC parameter for phonon mode i, g_i is mode degeneracy, ω_i is mode energy, γ_i is linewidth, and $N_{\epsilon f}$ is the electronic density of states at the Fermi surface. As an approximation at 5.6 K with $g = 1$ and $N_{\epsilon f} = 3.13/\text{eV}$ unit cell [41], we get $\lambda = 0.07$ for the A_g-4 mode, which is rather small compared to the reported $\lambda_{ep} \sim 0.453$ estimated from the transport measurement [11]. The Fano line shape exists through the whole temperature range, which means that an EPC exists in this material. The λ calculated near T_c suggests the contribution of the A_g-4 mode with the Fano line shape alone is insufficient to drive superconductivity. Since the Raman scattering experiment employed in this paper can only directly measure the Raman-active phonon modes, we are unable to directly demonstrate that Raman-inactive optical modes and/or optical modes at other parts of the BZ have a significant contribution to superconductivity. So, more work needs to be carried out to clarify the relationship of superconductivity and optical modes at other parts of the BZ in WP.

IV. DISCUSSION

Previous studies indicate that the anisotropic H_{c2} reaches maximum along the b-axis direction [11] and the vibration mode of acoustic branch phonon B_{3u} is strong in this direction by first-principles calculations in Fig. 4, which may be related to superconductivity. As the magnetic field increases, the T_c shifts to a lower temperature and the superconductivity is completely suppressed at $\mu_0 H = 12.5$ mT [11]. The superconducting transition shifts to a higher field with the external magnetic field rotating from the perpendicular ($\theta = 0°$ $E \perp b$-axis) to parallel ($\theta = 90°$, $E \parallel b$-axis) direction. The WP sample is along b-axis direction when $\theta = 90°$, thus H_{c2} is
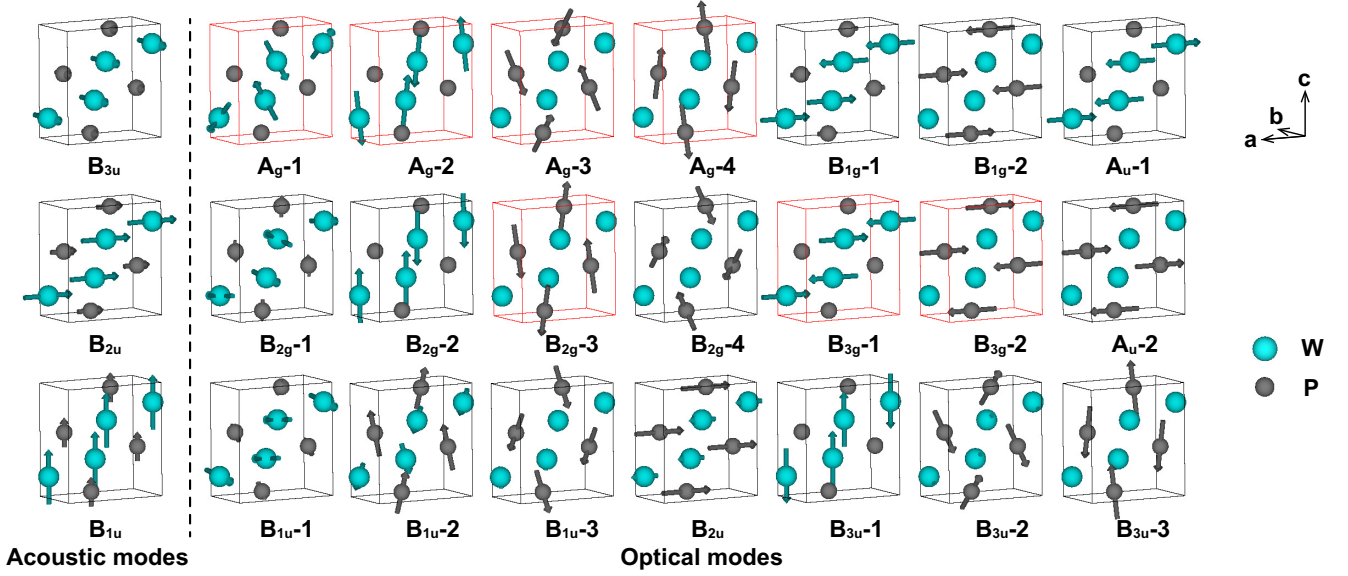
FIG. 4. Phonon vibration patterns for the acoustic and optical phonon modes in WP, which are determined from the DFT-based lattice dynamics calculations. The W and P atoms in the unit cell are denoted by blue and black spheres, respectively. The atomic displacements of the W and P atoms are indicated by the colored arrows.

highest in the *b*-axis direction. We can see in Fig. 4 that the vibration mode of the acoustic branch phonon B_{3u} is along the *b*-axis direction. Acoustic phonons are thought to contribute more to the total EPC λ. The relationship between the strength of EPC and superconductivity could be obtained by first-principles calculations. We calculate the electronic structure of WP. The orbital-resolved band structure and the electronic density of state (DOS) is shown in Figs. 5(a) and 5(b). DOS is mainly contributed by the W *d*-state in the energy range from -3 to 3 eV. W $5d$ states make the largest contribution to the electronic density of states at the Fermi level. Figure 5(c) shows the resolved phonon spectra in terms of the displacement directions of W and P atoms, in agreement with the projected phonon density of states (PhDOS) [Fig. 5(d)]. The heaviest atom W mainly contributes to the phonon spectrum in the low-frequency range from 0 up to 200 cm^{-1}, atom P contributions significantly to the high-frequency range from 300 to 400 cm^{-1}. The results of phonon dispersion and Ph-DOS of WP are highly consistent with previous theoretical calculations [13]. In the range of low-frequency from 0 to 200 cm^{-1}, the PhDOS are mainly attributed to the W atoms. The superconductivity of the WP was further investigated within the BCS and Migdal-Eliashberg theories [42,43] framework. To examine the contribution to λ from individual phonon modes, the mode-resolved EPC λ_{qv} can be calculated by

$$\lambda_{qv} = \frac{\gamma_{qv}}{\pi \hbar N(E_{\mathrm{F}})\omega_{qv}^2}, \qquad (8)$$

where γ_{qv}, ω_{qv}, and $N(E_F)$ are the phonon linewidths, the frequency of a lattice vibration with crystal momentum **q** in the branch **ν**, and the DOS at the Fermi level, respectively. Additionally, the phonon linewidths γ_{qv} can be

estimated by [44]

$$\gamma_{qv} = \frac{2\pi \omega_{qv}}{\Omega_{\mathrm{BZ}}} \sum_{k,n,m} \left| g^{v}_{kn,k+qm} \right|^2 \delta(\epsilon_{kn} - \epsilon_{\mathrm{F}})\delta(\epsilon_{k+qm} - \epsilon_{\mathrm{F}}), \quad (9)$$

where Ω_{BZ} is the volume of BZ, ϵ_{kn} and ϵ_{k+qm} are the Kohn-Sham energy, ϵ_F is the Fermi energy and $g^{v}_{kn,k+qm}$ denotes the EPC matrix element. Moreover, according to the linear response theory, the $g^{v}_{kn,k+qm}$ can be determined self-consistently. Subsequently, the Eliashberg electron-phonon spectral function $\alpha^2 F(\omega)$ and the cumulative frequency-dependent EPC function $\lambda(\omega)$ can be calculated by

$$\alpha^2 F(\omega) = \frac{1}{2\pi N(E_{\mathrm{F}})} \sum_{qv} \frac{\gamma_{qv}}{\omega_{qv}} \delta(\omega - \omega_{qv}) \qquad (10)$$

and

$$\lambda(\omega) = 2 \int_0^{\omega} \frac{\alpha^2 F(\omega)}{\omega} d\omega, \qquad (11)$$

respectively.

The logarithmic average frequency ω_{log} and the superconducting transition temperature T_c can be calculated as follows [45–47]:

$$\omega_{\mathrm{log}} = \exp\left[\frac{2}{\lambda} \int_0^{\infty} \frac{d\omega}{\omega} \alpha^2 F(\omega) \ln\omega \right] \qquad (12)$$

and

$$T_c = \frac{\omega_{\mathrm{log}}}{1.2} \exp\left[-\frac{1.04(1+\lambda)}{\lambda - \mu^*(1+0.62\lambda)}\right], \qquad (13)$$

where μ^* is defined as the effective screened Coulomb repulsion.

Figure 5(e) shows that the relatively large strength of the EPC (labeled by λ_{qv}) is related to the low-frequency phonon modes (0–200 cm^{-1}). These low-frequency phonon modes
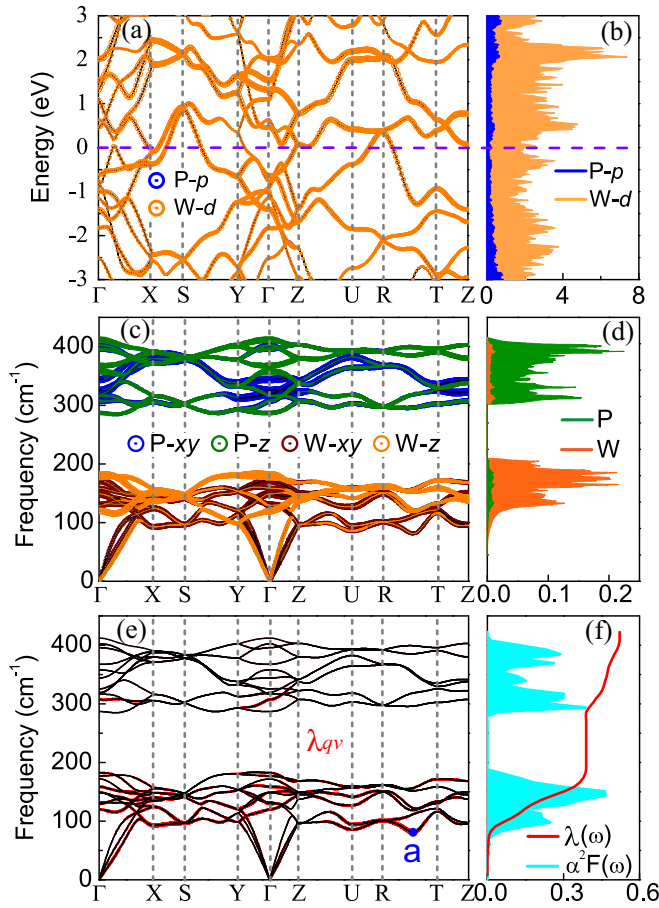
FIG. 5. (a) Calculated electronic band structure of WP along the high-symmetry directions of q points ($\Gamma \rightarrow X \rightarrow S \rightarrow Y \rightarrow \Gamma \rightarrow Z \rightarrow U \rightarrow R \rightarrow T \rightarrow Z$). We plot in the energy range from -3 to $+3$ eV. (b) The projection of the P p-orbital and W d-orbital. The Fermi level is set at zero energy. (c) The phonon spectra of WP resolved in terms of the vibration directions of W and P atoms. (d) PhDOS for WP. (e) The magnitude of the EPC λ_{qv}. (f) The Eliashberg spectral function $\alpha^2 F(\omega)$ and the cumulative frequency-dependent EPC $\lambda(\omega)$.

that stem from the W-z and W-xy vibrations make a significant contribution to the cumulative frequency-dependent EPC function $\lambda(\omega)$. The Eliashberg spectral function $\alpha^2 F(\omega)$ reveals that the two major peaks in the low-frequency region of 0–200 cm^{-1} lead to a rapid increase of the cumulative $\lambda(\omega)$ [Fig. 5(f)], confirming the jump of the total EPC in this range and pointing to a medium-coupling superconductor with a $\lambda = 0.514$. Below 200 cm^{-1}, vibration modes (12 phonon modes) of the spectral function $\alpha^2 F(\omega)$ contribute to around 76% of the strength for λ and vibration modes (12 phonon modes) between 250 cm^{-1} and up to 450 cm^{-1} are responsible for the rest of the strength for λ. In particular, acoustic branches contribute about 30% of the strength for λ. The out-of-plane (ZA), in-plane transverse (TA), and in-plane longitudinal (LA) modes constitute the three acoustic branches for WP. LA and ZA soft-mode vibrations of W

atoms may play a major role in Fig. 5(e), especially at the largest soft mode at point a. Such superconductivity of WP is mainly attributed to the low-frequency phonon modes (0–200 cm^{-1}) originating from the motion of W atoms. Based on the McMillian-Allen-Dynes formula, the superconducting transition temperature T_c is evaluated to be 0.84 K with $\mu^* = 0.17$, which is consistent with the experimental results [11]. In IrGe, another 5d MnP-type structure superconductor with $T_c = 4.7$ K, a low-frequency phonon is also found to contribute the most of the total EPC λ by specific-heat measurement [48]. Consistent with that experimental result, theoretical calculations by Tütüncü *et al.* [49] indicate that the low-frequency modes below 3.8 THz (127 cm^{-1}) contribute up to around 76% to the EPC λ. Furthermore, spin-orbit coupling (SOC) leads to the hardening of low-frequency phonon modes, which reduce the EPC. The SOC of IrGe is mainly associated with an Ir atom which possesses a 5d orbital and much heavier mass than that of a Ge atom. Therefore, the emergence of superconductivity in WP is similar to IrGe, which originates from low-frequency phonons contributed by 5d atoms.

V. CONCLUSION

In conclusion, we investigated the contribution of different phonon modes to the EPC of the transition-metal pnictide superconductor WP. The frequencies of Raman-active phonon modes measured in WP are in good agreement with the theoretical calculations. We have analyzed the A_g and B_{3g} modes with the help of ARPRS under parallel- and cross-polarized configurations. A Fano line shape was observed for the A_g-4 mode from 5.6 to 300 K, which contributes little to the superconductivity with a small strength of EPC estimated from Allen's formula. Compared with the phonon dispersion obtained by first-principles calculations, we found the superconductivity mainly originated from the low-frequency phonon modes below 200 cm^{-1} resulting from the motion of W atoms. The results in our paper can help us to understand superconductivity in transition-metal pnictides with the MnP structure.

[1] Y. Kamihara, T. Watanabe, M. Hirano, and H. Hosono, J. Am. Chem. Soc. **130**, 3296 (2008).

[2] B. Y. Pan, H. Jang, J.-S. Lee, R. Sutarto, F. He, J. F. Zeng, Y. Liu, X. W. Zhang, Y. Feng, Y. Q. Hao, J. Zhao, H. C. Xu, Z. H. Chen, J. P. Hu, and D. L. Feng, Phys. Rev. X **9**, 021055 (2019).

[3] Q. Niu, W. C. Yu, K. Y. Yip, Z. L. Lim, H. Kotegawa, E. Matsuoka, H. Sugawara, H. Tou, Y. Yanase, and Swee K. Goh, Nat. Commun. **8**, 15358 (2017).

[4] D. J. Campbell, J. Collini, J. Sławińska, C. Autieri, L. Wang, K. Wang, B. Wilfong, Y. S. Eo, P. Neves, D. Graf, E. E. Rodriguez, N. P. Butch, M. Buongiorno Nardelli, and J. Paglione, npj Quantum Mater. **6**, 38 (2021).

[5] N. Jiang, Y. Nii, H. Arisawa, E. Saitoh, and Y. Onose, Nat. Commun. **11**, 1601 (2020).

[6] N. Jiang, Y. Nii, H. Arisawa, E. Saitoh, J. Ohe, and Y. Onose, Phys. Rev. Lett. **126**, 177205 (2021).

[7] W. Wu, J.-G. Cheng, K. Matsubayashi, P. Kong, F. Lin, C. Jin, N. Wang, Y. Uwatoko, and J. Luo, Nat. Commun. **5**, 5508 (2014).

[8] W. Tremel, R. Hoffmann, and J. Silvestre, J. Am. Chem. Soc. **108**, 5174 (1986).

[9] D. Hirai, T. Takayama, D. Hashizume, and H. Takagi, Phys. Rev. B **85**, 140509(R) (2012).

[10] J.-G. Cheng, K. Matsubayashi, W. Wu, J. P. Sun, F. K. Lin, J. L. Luo, and Y. Uwatoko, Phys. Rev. Lett. **114**, 117001 (2015).

[11] Z. Y. Liu, W. Wu, Z. Z. Zhao, H. C. Zhao, J. Cui, P. F. Shan, J. H. Zhang, C. L. Yang, P. J. Sun, Y. Wei, S. L. Li, J. G. Zhao, Y. Sui, J. G. Cheng, L. Lu, J. L. Luo, and G. T. Liu, Phys. Rev. B **99**, 184509 (2019).

[12] G. Cuono, F. Forte, M. Cuoco, R. Islam, J. L. Luo, C. Noce, and C. Autieri, Phys. Rev. Materials **3**, 095004 (2019).

[13] C. Tayran and M. Cakmak, J. Appl. Phys. **126**, 175103 (2019).

[14] X. L. Liu, X. Zhang, M. L. Lin, and P. H. Tan, Chin. Phys. B **26**, 067802 (2017).

[15] P. M. Nikolic, P. L. Miljkovic, B. Mihajlovic, and B. Lavrencic, J. Phys. C: Solid State Phys. **10**, L289 (1977).

[16] O. S. Vereshchagin, D. V. Pankin, M. B. Smirnov, N. S. Vlasenko, V. V. Shilovskikh, and S. N. Britvin, J. Alloys Compd. **853**, 156468 (2021).

[17] P. Hohenberg and W. Kohn, Phys. Rev. **136**, B864 (1964).

[18] W. Kohn and L. J. Sham, Phys. Rev. **140**, A1133 (1965).

[19] G. Kresse and J. Furthmüller, Phys. Rev. B **54**, 11169 (1996).

[20] J. P. Perdew, K. Burke, and M. Ernzerhof, Phys. Rev. Lett. **77**, 3865 (1996).

[21] G. Kresse and D. Joubert, Phys. Rev. B **59**, 1758 (1999).

[22] H. J. Monkhorst and J. Pack, Phys. Rev. B **13**, 5188 (1976).

[23] A. Togo and I. Tanaka, Scr. Mater. **108**, 1 (2015).

[24] S. Baroni, S. De Gironcoli, A. Dal Corso, and P. Giannozzi, Rev. Mod. Phys. **73**, 515 (2001).

[25] J. Bardeen, L. N. Cooper, and J. R. Schrieffer, Phys. Rev. **108**, 1175 (1957).

[26] D. R. Hamann, Phys. Rev. B **88**, 085117 (2013).

[27] X. Wang, Y. Li, L. Huang, X. W. Jiang, L. Jiang, H. Dong, Z. Wei, J. Li, and W. Hu, J. Am. Chem. Soc. **139**, 14976 (2017).

[28] Z. Tian, C. Guo, M. Zhao, R. Li, and J. Xue, ACS Nano **11**, 2219 (2017).

[29] X. Xu, Q. Song, H. Wang, P. Li, K. Zhang, Y. Wang, K. Yuan, Z. Yang, Y. Ye, and L. Dai, ACS Appl. Mater. Interfaces **9**, 12601 (2017).

[30] U. Fano, Phys. Rev. **124**, 1866 (1961).

[31] F. Cerdeira, T. A. Fjeldly, and M. Cardona, Phys. Rev. B **8**, 4734 (1973).

[32] S. F. Wu, P. Richard, X. B. Wang, C. S. Lian, S. M. Nie, J. T. Wang, N. L. Wang, and H. Ding, Phys. Rev. B **90**, 054519 (2014).

[33] K. Sen, Y. Yao, R. Heid, A. Omoumi, F. Hardy, K. Willa, M. Merz, A. A. Haghighirad, and M. Le Tacon, Phys. Rev. B **100**, 104301 (2019).

[34] S. L. Cooper, M. V. Klein, B. G. Pazol, J. P. Rice, and D. M. Ginsberg, Phys. Rev. B **37**, 5920(R) (1988).

[35] V. Magidson and R. Beserman, Phys. Rev. B **66**, 195206 (2002).

[36] W.-L. Zhang, H. Li, D. Xia, H. W. Liu, Y.-G. Shi, J. L. Luo, J. P. Hu, P. Richard, and H. Ding, Phys. Rev. B **92**, 060502(R) (2015).

[37] D. Chen, Y.-L. Jia, T.-T. Zhang, Z. Fang, K. Jin, P. Richard, and H. Ding, Phys. Rev. B **96**, 094501 (2017).

[38] P. B. Allen, Phys. Rev. B **6**, 2577 (1972).

[39] J. Winter and H. Kuzmany, Phys. Rev. B **53**, 655 (1996).

[40] Z. V. Popović, Z. D. Dohčević-Mitrović, N. Paunović, and M. Radović, Phys. Rev. B **85**, 014302 (2012).

[41] Topological Materials Database, https://topologicalquantumchemistry.org/#/.

[42] E. R. Margine and F. Giustino, Phys. Rev. B **87**, 024505 (2013).

[43] F. Giustino, Rev. Mod. Phys. **89**, 015003 (2017).

[44] M. M. Dacorogna, M. L. Cohen, and P. K. Lam, Phys. Rev. Lett. **55**, 837 (1985).

[45] W. L. McMillan, Phys. Rev. **167**, 331 (1968).

[46] P. B. Allen and R. C. Dynes, Phys. Rev. B **12**, 905 (1975).

[47] P. B. Allen and R. C. Dynes, J. Phys. C: Solid State Phys. **8**, L158 (1975).

[48] D. Hirai, M. N. Ali, and R. J. Cava, J. Phys. Soc. Jpn. **82**, 124701 (2013).

[49] H. M. Tütüncü, H. Y. Uzunok, E. Karaca, S. Bağcı, and G. P. Srivastava, Intermetallics **106**, 107 (2019).